J Nanopart Res (2020) 22: 31
https://doi.org/10.1007/s11051-019-4749-1

RESEARCH PAPER

Catalysis of sugarcane-bagasse pyrolysis by Co, Ni, and Cu single and mixed oxide nanocomposites

Mahmoud Mohamed Emara · **Shrouq Hossam Ali** · **Taher Salah Edin Kassem** · **P. Gregory Van Patten**

Received: 11 September 2019 / Accepted: 30 December 2019 / Published online: 13 January 2020

Abstract Pyrolysis of biomass is an important process in which renewable biological waste is converted to energy products and preliminary chemicals. Therefore, various types of catalysts, including metal oxides, have been investigated for more efficient and selective biomass pyrolysis. Co, Ni, and Cu single and mixed metal oxide (SMO and MMO) nanoparticles (NPs) of 3 to 47 nm were synthesized, characterized, and studies for their catalytic activities towards pyrolysis of sugarcane bagasse (PSCB). After mixing the oxide NPs with bagasse, thermogravimetry was performed at a heating rate of 5 °C/min from ambient temperature to 600 °C. Thermogravimetric analysis followed by kinetic calculations of the activation energy through Coats−Redfern model show that all oxide NPs of this study exhibit catalytic activity towards cellulose and hemicellulose thermal degradation during PSCB, in the order MMO > SMO. Cu-containing SMO and MMO NPs show exceptional catalytic activities compared to their analogues. On the other hand, lignin degradation kept proceeding over a wide range of high temperature, just like that of the plain PSCB. This is considered selective enhancement of the catalysis of cellulose and hemicellulose thermal degradation versus lignin degradation, which is promising for improving the composition and quality of PSCB products. Only Cu-containing double and triple MMOs were so catalytically active that they catalyzed lignin degradation along with the cellulose and hemicellulose.

Keywords Bagasse · Cellulose · Oxides · Nanocomposites · Thermogravimetry · Catalysis

Abbreviations

BET	Brunauer–Emmett–Teller
DTG	Derivative thermogravimetry
FWHM	Full width at half maximum
ICP-AES	Inductively coupled plasma atomic emission spectroscopy
JCPDS	Joint Committee on Powder Diffraction Standards
MMO	Mixed metal oxide
NPs	Nanoparticles
PSCB	Pyrolysis of sugarcane bagasse
SCB	Sugarcane bagasse
SMO	Single metal oxide
TEM	Transmission electron microscopy
TG	Thermogravimetry
XRD	X-ray diffraction

Electronic supplementary material The online version of this article (https://doi.org/10.1007/s11051-019-4749-1) contains supplementary material, which is available to authorized users.

M. M. Emara (✉) · S. H. Ali · T. S. E. Kassem
Chemistry Department, Faculty of Science, Alexandria University, P.O. Box 426, Ibrahimia, Alexandria 21321, Egypt
e-mail: mahmoud.emara@alexu.edu.eg

P. G. Van Patten
Department of Chemistry, Middle Tennessee State University, Murfreesboro, TN 37132, USA

Introduction

The escalating worldwide demand for energy necessitates exploration of renewable energy sources. Biomass is a renewable, non-fossil energy source that comprises biodegradable organic matter. Biomass is found in diverse forms including agriculture residues and algae (Cen et al. 2019; Janke et al. 2019; Lopez-Rodriguez et al. 2019; Mohapatra et al. 2019). Several thermal conversion processes have been developed to produce energy from biomass (Deboni et al. 2019; Ikaheimo et al. 2019; Khiari et al. 2019; Prager et al. 2019; Thomas et al. 2019). Pyrolysis is an important process to convert biomass to energy products such as valuable bio-oil (Dhanalakshmi and Madhu 2019), gases (Bedoic et al. 2019; Dahunsi 2019), and char (Paunovic et al. 2019). Sugarcane bagasse (SCB) is one of most abundant agriculture residues that can be used as an energy renewable source. The bio-oil and char produced from the PSCB has calorific value higher than that of the original bagasse. SCB is mainly composed of cellulose, hemicellulose, and lignin in addition to traces of inorganic minerals and organic extracts (Said et al. 2013). Variation in the components of SCB results in complicated pyrolysis processes and variation in the biofuel yield (Motaung and Anandjiwala 2015). Catalytic pyrolysis has been identified as a possible way to improve the selectivity and upgrade the desired product (Li et al. 2019; Ozbay et al. 2019; Weldekidan et al. 2019), and the catalyst is expected to directly impact the product yield (Elbaba and Williams 2013; Hassan et al. 2016). Pyrolysis of hemicellulose and cellulose produces mainly volatile and liquid products of low and moderate molecular weights (desired), with very little solid char (undesired) (Shen et al. 2010). On the other hand, char is a major product of lignin pyrolysis (Stefanidis et al. 2014). For this reason, a catalyst is sought that selectively and efficiently catalyzes the pyrolysis of hemicellulose and cellulose and hinders the pyrolysis of lignin during the process of PSCB.

In the recent years, metal oxide nanocatalysts have attracted attention due to their efficient catalytic performance compared to their bulk analogues (Ali et al. 2018; Li et al. 2018; Ma et al. 2019; Muthuvinothini and Stella 2019). They have unique properties including magnetic, optical, dielectric, and redox properties, along with large surface area, high stability and reusability, which in turn increase the catalyst efficiency. Accordingly, they have a broad spectrum of applications (Ali et al. 2018; Banković-Ilić et al. 2017; Gnanasekaran et al. 2017; Li et al. 2017; Li et al. 2018; Ma et al. 2019; Muthuvinothini and Stella 2019). MMOs are oxides which contain two or more different types of metal cations. As catalysts, they are known of enhanced durability, catalytic activity, and selectivity (Gawande et al. 2012). The diversity of the metal ions inside the MMO crystal provides various oxidation states with different coordination capacities, giving the surface a multifunctional nature (Hassan and Tammam 2018; Khan et al. 2017; Liu et al. 2013). MgO, CaO, NiO, and CuO separately showed selective catalytic PSCB for the production of gases and liquids (Kuan et al. 2013). MMOs such as zeolite and its derivatives have recently been widely studied as catalysts for the PSCB and proved to give excellent results (Balasundram et al. 2018a, b; Cardoso et al. 2019; Ghorbannezhad et al. 2018; Ghorbarmezhad et al. 2018). ZSM-5 is a common type of zeolites composed of Na, Al, and Si mixed oxides (Kumar et al. 2015). Sometimes, ZSM-5 was used as a bare catalyst (Cardoso et al. 2019; Ghorbannezhad et al. 2018; Ghorbarmezhad et al. 2018), and in others, it carried a promoter (Balasundram et al. 2018a, b).

To the best of our knowledge, the spectrum of MMOs studied in the catalysis of PSCB is limited. The purpose of the present study is to investigate the catalytic efficiency of Cu, Co, and Ni SMO NPs and their corresponding double and triple MMO NPs on the PSCB at low heating rate. Thermogravimetric analysis and kinetic study were conducted to investigate the catalytic activity and any synergetic behavior that may occur. The catalysts were well characterized to investigate possible correlations between their chemical and physical status with their catalytic nature.

Experimental

Materials

Copper (II) acetate monohydrate ($Cu(OAc)_2{\cdot}H_2O$) (OXFORD laboratory reagent, 95%). Nickel acetate tetrahydrate ($Ni(OAc)_2{\cdot}4H_2O$) (Qualikems laboratory reagent, 98%) cobaltous acetate tetrahydrate ($Co(OAc)_2{\cdot}4H_2O$) (BDH Chemicals Ltd., Poole England, 99.5%). Sodium hydroxide pellets (NaOH) (LOBA CHEMIE Laboratory Reagent and Fine Chemicals, Mumbai, India). Acetic acid glacial (CH_3COOH) (LOBA CHEMIE Laboratory Reagent and Fine Chemicals, Mumbai, India, 99%). Sugarcane bagasse (SCB) was supplied from a near village Qus, Qina Governate, Upper Egypt. All the chemicals were used without further purification and distilled water was used throughout this study.

Sugarcane bagasse

The sugarcanes were pressed to remove excess liquid content, and the resulting biomass was washed 10 times with distilled water, and then dried in the oven at 50 °C for 24 h. The resulting dry stalks were ground with a mill into a fine powder with average particle size of about 0.5 mm. The bagasse powder was sieved to remove particles larger than 1 mm (see Fig. S1 in the supplementary information).

Synthesis and characterization of metal oxide NPs

Synthesis of Cu SMO NPs

The synthesis of Cu SMO NPs was adapted from a previously published procedure (Zhu et al. 2011). In a 1000 mL round-bottom flask, 24 g (0.12 mol) of copper acetate was dissolved in 600 mL distilled water and 2 mL glacial acetic acid. The solution was heated to boiling with magnetic stirring, and then 30 mL of 8 M aqueous NaOH was added onto the boiling solution. The color converted immediately from blue to black and a black suspension was produced. The solution was refluxed for 2 h, after which the heat was removed, and the mixture was cooled to the room temperature. CuO precipitate was centrifuged and washed several times with distilled water. CuO NPs were calcined at 450 °C for 4 h. This procedure is based on the following sequence of chemical reactions:

$$Cu^{2+}\ (aq) + 2\ OH^{-}\ (aq) \rightarrow Cu(OH)_2\ (s) \tag{1}$$

$$Cu(OH)_2\ (s) \overset{\Delta}{\rightarrow} CuO\,(s) + H_2O\,(l) \tag{2}$$

Synthesis of other SMO and MMO NPs

The same above procedure was followed, except that cobalt (II) acetate and nickel (II) acetate were substituted in place of copper (II) acetate according to the masses given in Table 1.

Characterization of the synthesized NPs

The crystal structure, composition, and average crystal size of the prepared NPs were determined with powder x-ray diffraction. Measurements were made on a Bruker AXS D8 with Cu Kα radiation (λ = 1.54060 Å) over a range of 2θ = 10°–80° using a scan speed of 2°/ min. The morphology and particle sizes were examined by transmission electron microscopy (TEM) using a JEOL 2100 TEM (Japan) with an accelerating voltage of 200 kV. The specific surface area of the prepared nanoparticles was determined through Brunauer–Emmett–Teller (BET) technique on a NOVA 3200 surface area analyzer. Quantitative elemental analysis of the metals in the MMO NPs was performed via inductively coupled plasma atomic emission spectroscopy (ICP-AES) on an Agilent ICP-OES 5100 VDV with RF power 1.2 kW, nebulizer flow 0.7 L/min, and plasma flow 12 L/min.

Catalytic activity

Thermogravimetry was conducted to investigate the catalytic activity of single, double, and triple MMO NPs on PSCB. The sample was prepared by mixing the NPs (either SMO or MMO) with SCB so that the NPs were 10 wt% of the whole sample mass. Physical mixing was used until homogenous color was achieved. Thermal decomposition of SCB with different SMO and MMO NPs was monitored using a SDT Q600 V20.9 thermogravimetric analyzer. The experiment proceeded under inert atmosphere as the sample was flushed with constant flow of 20 mL/min N_2 to avoid sample oxidation and any gaseous or condensable product to be gathered. The

Table 1 Mole fractions and weights of the metal acetates added during the synthesis

	$Co(Ac)_2.4H_2O$ (Mw 249.1)		$Ni(Ac)_2.4H_2O$ (Mw 248.8)		$Cu(Ac)_2.H_2O$ (Mw 199.7)	
	x	wt (g)	y	wt (g)	1-x-y	wt (g)
Co	1.0	14.9	0.0	0.0	0.0	0.0
Ni	0.0	0.0	1.0	14.9	0.0	0.0
Cu	0.0	0.0	0.0	0.0	1.0	12.0
Co-Ni	0.5	7.5	0.5	7.5	0.0	0.0
Co-Cu	0.5	7.5	0.0	0.0	0.5	6.0
Ni-Cu	0.0	0.0	0.5	7.5	0.5	6.0
Co-Ni-Cu	0.3	4.5	0.3	4.5	0.4	4.8

sample was heated from ambient temperature to 600 °C with heating rate of 5 °C/min. At the end of the process, the weight loss was recorded by thermobalance.

Results and discussion

Characterizations of the prepared NPs

X-ray diffraction

XRD patterns of the NPs are shown in Fig. 1. In the case of copper oxide NPs, all the observed peaks can be indexed to monoclinic CuO (JCPDS no. 80–1916) with no extra peaks from impurities such as Cu_2O, $Cu(OH)_2$ or other precursor compounds. Diffraction patterns from nickel oxide and cobalt oxide NPs also match the standard patterns for NiO and Co_3O_4 single phases (JCPDS no. 04-0835 and JCPDS no. 42-1467), respectively.

Investigating the diffraction peaks for the double and triple MMO NPs shows that they are a mixture of their corresponding SMOs. Comparing with the XRD patterns of the SMOs shows slight peak shifts (Table S1 in the supplementary information) for the MMOs, which means changes in the interplanar distances (d). These changes result from doping and formation of phases made of more than one metal (mixed phases). The FWHM (full width at half maximum) of the most intense diffraction peaks were measured in order to estimate the average crystal domain size (D_{XRD}) using Debye-Scherrer equation. The observed peak widths are consistent with the nanometer scale nature of the crystals. Table 2 shows D_{XRD} values of the SMO and MMO NPs, where they all seem to lie within the same range of 3 to 47 nm.

Elemental analysis

ICP-AES analysis of the double and triple MMO NPs shows that the precipitated metal ratios are very close to those added during the synthesis (Table 2).

TEM analysis

Figure 2 a shows that the majority of CuO NPs are spherical while some are irregular with larger sizes. NiO NPs (Fig. 2b) take spherical, hexagonal, and square shapes, while Co_3O_4 NPs (Fig. 2c) are irregular in shape.

MMO NPs (Fig. 2d–g) varied between spherical and irregular shapes. We assume that the relatively small shapes are the SMO NPs owing to their resemblance with the results of Fig. 2a–c, and the large shapes are the MMO NPs.

A summary of the morphology and the average particles sizes calculated from TEM (D_{TEM}) for the SMO and MMO NPs are tabulated in Table 2. The average particle sizes are in relative agreement with the results calculated by Scherrer equation (in the same table). Some NPs look slightly larger in the TEM images than XRD calculations, which indicate that the crystal grain size may be even smaller than the particle size.

Looking at the size ranges calculated from the TEM images and comparing those of the SMO, double MMO, and triple MMO NPs, one can see that the sizes become smaller as the number of constituting metals in the MMO increases. The upper limit of the size ranges decreases from 40s, 30s, to 20 nm for SMO, double MMO, and triple MMO NPs, respectively. This phenomenon agrees with the results reported in the literature, where doping has a considerable effect on the morphology of the synthesized NPs (Yang et al. 2010).

Surface area

As given in Table 2, the specific surface area of the metal oxide NPs takes the following trend double MMO NPs < SMO NPs < Triple MMO NPs. This trend does not correlate to the sizes, which may be due to possible aggregations that overcome the effect of the particle sizes on their surface area. According to a previous work by our group, aggregation of the NPs has a negative effect on the surface area and accordingly the catalytic activity, regardless of the crystallite size (Ismail et al. 2017).

Evaluation of the catalytic activity of SMO and MMO NPs on the PSCB

PSCB without metal oxide NPs

The thermogravimetric (TG) curve given in Fig. 3 (dashed line) describes the thermal decomposition of SCB without NPs in two mass-loss stages. Each peak in the derivative thermogravimetry (DTG) curve (solid line in Fig. 3) represents a mass-loss step in the TG curve (Garcıa-Perez et al. 2001; Mothé and de Miranda 2009). The first stage of mass loss occurred from 33 to 76 °C (step a in the DTG curve) is due to evaporation of the entrapped moisture and light volatile compounds. The second stage of mass loss takes place between 177

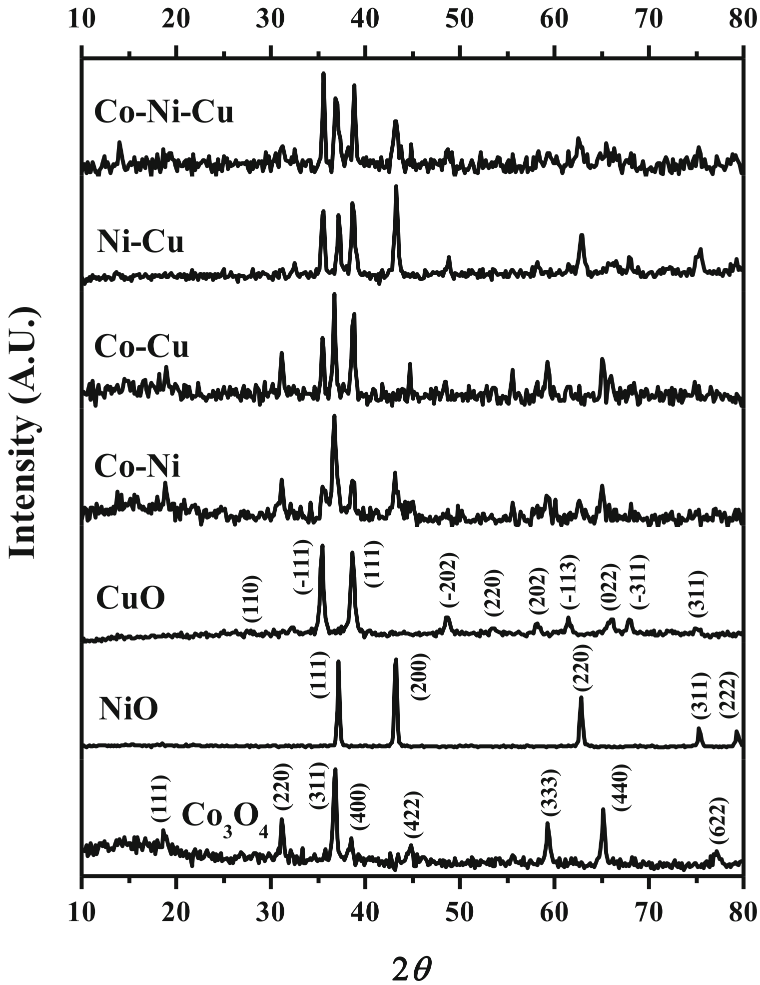

Fig. 1 XRD patterns of Co, Ni, and Cu SMO NPs and their corresponding double and triple MMO NPs

and 539 °C, and it corresponds to the process of PSCB itself, where 177 °C is the initial temperature at which pyrolysis starts (T_i) and 539 °C is the final temperature at which thermal degradation ceases (T_f). This stage consists of four overlapping DTG steps. The first and second steps (b and c in the DTG curve) almost lie between 177 and 298 °C and correspond to hemicellulose decomposition. The third step (d in the DTG curve) represents the major mass loss, which is due to the decomposition of cellulose (El-Sayed and Mostafa 2015). At the maximum of this peak, the rate of mass loss with respect to temperature change reaches maximum. The temperature at this maximum is referred to as T_m, which happens to be 345 °C for the SCB of this study. The fourth step (e in the DTG curve) relates to lignin decomposition and seems to take place over a wide range of high temperature (Garcıa-Perez et al. 2001).

Lignin decomposition is very difficult because of its polymeric complexity. Therefore, it usually occurs at temperatures slightly interfering with degradation of hemicellulose and cellulose decomposition and beyond. It is the step responsible for the charring and residue production resulting from PSCB (Mortari et al. 2010). Presence of residual mass at 600 °C refers to incomplete lignin pyrolysis. The very shallow slope of the DTG curve starting from 450 °C indicates very slight lignin decomposition, which results in the presence of the residual mass at the end of the run.

Degradation of cellulose and hemicellulose during PSCB in presence of the NPs

Figure 4 a shows the TG curves of PSCB in absence and presence of the SMO and MMO NPs over the whole temperature range of the conducted TG experiment

Table 2 Elemental analysis (according to ICP), phases, average crystallite sizes (according to XRD and TEM), shapes, the specific surface areas (according to BET), DTG temperatures (initial, maximum rate, and final), correlation coefficient of Coats-Redfern linear fit, order of the reaction of the PSCB according to Coats-Redfern linear fit, and the activation energies of the PSCB; all in absence and presence of the SMO and MMO NPs

Sample	Metal mole fractions acc. to ICP			Phase	Range of particles size for each ratio (nm)		Shape of particles	sp. surface area (m^2/g)	T_i	T_m	T_f	R^2	*n*	*Ea* (KJ/mol)
	Co	Ni	Cu		D_{XRD}	D_{TEM}								
SCB	–	–	–	–	–	–	–	–	177	345	539	0.98	2	105
Co	–	–	–	Co_3O_4	3–42	48–105	Irregular	254	177	336	UIT	0.97	2	85
Ni	–	–	–	NiO	11–47	18–38	Spherical, hexagonal quadruple	203	177	340	UIT	0.98	2	95
Cu	–	–	–	CuO	3–29	26–52	Spherical, irregular	173	175	332	UIT	0.98	2	84
Co-Ni	0.478	0.522	0.000	Co_3O_4, doped Co_3O_4, NiO, and UIP	11–28	17–67	Irregular	168	181	334	UIT	0.97	2	80
Co-Cu	0.514	0.000	0.486	Co_3O_4, doped Co_3O_4, CuO, and doped CuO	3–34	20–54	Irregular	67	176	322	575	0.98	2	83
Ni-Cu	0.000	0.497	0.504	NiO, CuO, doped CuO	10–32	20–47	Spherical, irregular	107	178	321	563	0.97	2	82
Co-Ni-Cu	0.321	0.302	0.377	Co_3O_4, doped Co_3O_4, NiO, CuO, doped CuO	9–23	12–24	Spherical, irregular	390	179	321	553	0.98	2	76

UIT unidentified temperature, *UIP* unidentified phase

(room temperature to 600 °C). This relatively wide scale does not allow the reader to observe the fine differences between one oxide and another. Therefore, we rather focused on the mass changes within the range of 250–375 °C in Fig. 4b, which delivers the majority of the thermal decomposition. In Fig. 4b, T_m of the plain SCB was marked by a dotted vertical line passing through the whole figure to facilitate observation of any TG shifts with respect to temperature. Figure 4 b shows that addition of the metal oxide NPs results in shifts of mass losses towards lower temperatures, indicating a catalytic effect of metal oxide NPs on the thermal degradation of cellulose and hemicellulose (Ismail et al. 2017). Several publications in the literature report catalytic activity of various metal oxides on the pyrolysis of cellulose, cellulose derivatives, biomass, and bioproducts (Arregi et al. 2018; Chang et al. 2018; Donar and Sinag 2016; Hernando et al. 2017; Murugappan et al. 2016; Nguyen et al. 2016). The shifts become more pronounced upon changing from SMO to double MMO and finally to triple MMO NPs. This behavior reveals that the metal oxide NPs of this study have the following relative catalytic activity on the PSCB: triple MMO NPs > double MMO NPs > SMO NPs, as will be discussed below.

For more details and better understanding of the TG behavior, Figs. 5, 6, and 7 give the DTG curves in stretched scales covering the ranges 150–225 °C, 225–375 °C, and 375–600 °C, respectively. Figure 5 presents the DTG data at the beginning of the PSCB, and due to the noisy nature of this range, linear fitting was done to estimate T_i. The linear fitting and its results are shown in Fig. S2 and Table S2 in the supplementary information, respectively. Absence or presence of the NPs did not seem to affect T_i as all samples exhibited T_i between 175 and 181 °C, and no trend was observed.

Figure 6 and Table 2 show that addition of the SMO and MMO NPs caused T_m to decrease. These results are in good agreement with the literature and indicate a catalytic effect of the SMO and MMO NPs on the cellulose and hemicellulose thermal decompositions (Liu et al. 2008). The lowest T_m was within 322–321 °C in presence of Co-Cu, Ni-Cu, and Co-Ni-Cu MMO NPs. In other words, these three MMO NPs represent the highest catalytic activity towards thermal degradation of cellulose and hemicellulose during PSCB.

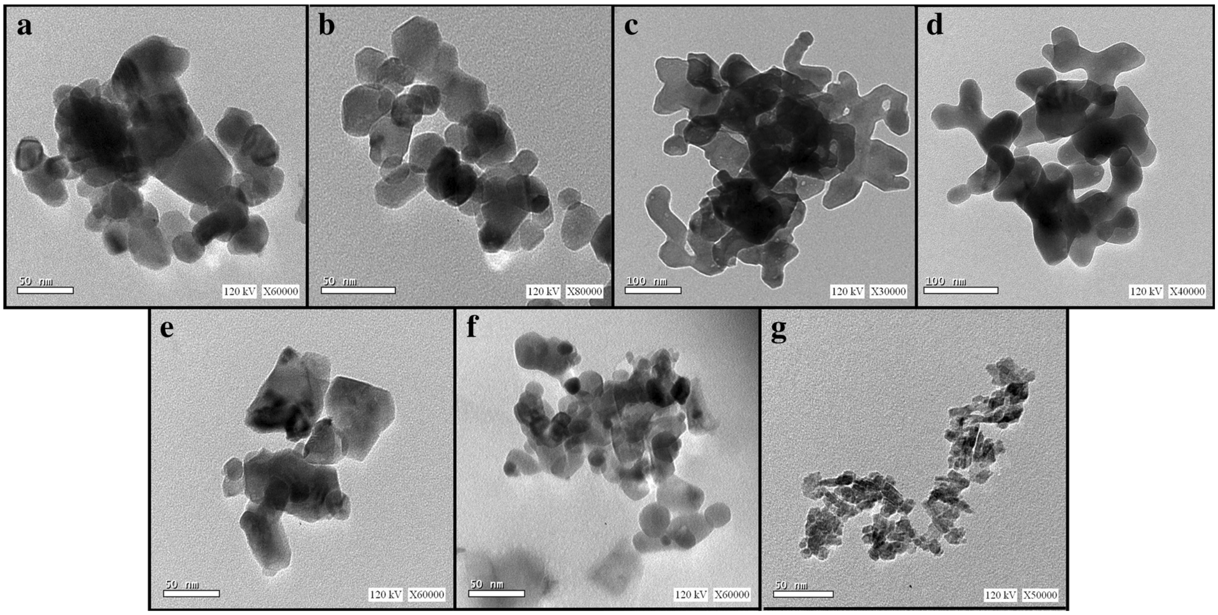

Fig. 2 TEM images of SMO NPs of **a** CuO, **b** NiO, **c** Co_3O_4, and MMO NPs of **d** Co-Cu, **e** Ni-Co, **f** Ni-Cu, and **g** Co-Ni-Cu

Degradation of lignin during PSCB in presence of the SMO and MMO NPs

Co-Cu, Ni-Cu, and Co-Ni-Cu MMO NPs notably catalyze lignin thermal degradation so that it appears in Fig. 7 as a DTG peak distinguishable from those of hemicellulose and cellulose. As shown in Fig. 7 and Table 2, lignin thermal decomposition in case of those three MMOs ends at T_f of 575, 563, 553 °C, respectively. The rest of SMO and MMO NPs do not make much difference in lignin decomposition in comparison with plain SCB, where lignin decomposition spreads over a wide range of high temperature, except that lignin decomposition kept proceeding and did not show T_f until 600 °C. At this point, it can be concluded that Co-Cu, Ni-Cu, and Co-Ni-Cu MMO NPs are so catalytically active that they catalyze thermal degradation of lignin with cellulose and hemicellulose. On the other hand, the rest of SMO and MMO NPs show less catalytic activity, yet they only catalyze cellulose and hemicellulose thermal degradation without doing so to lignin, which can be counted as selective catalysis.

Catalytic activity of the SMO NPs

Co_3O_4 NPs relatively resulted in more lowering in T_m than NiO NPs do. In other words, Co_3O_4 NPs are more catalytic for cellulose and hemicellulose thermal decompositions than NiO NPs. The presence of Co_3O_4 NPs shifted T_m from 345 °C to 336 °C, while NiO NPs shifted it down to 340 °C only. The reason of this slight difference could be due to the large specific surface area of Co_3O_4 NPs compared to NiO NPs (254 and 203 m^2/g, respectively, as shown in Table 2). Large surface area provides more contact between the catalyte (SCB) and the active sites of the catalyst (metal oxide NPs), promoting the decomposition of cellulose and hemicellulose to occur at lower temperature (Li et al. 2008). On the other hand, CuO NPs gave the highest catalytic activity (T_m 332 °C) among the three SMO NPs, despite Cu NPs having the lowest specific surface area (173 m^2/g), illustrating the compromise between the chemical nature and the specific surface area as factors affecting the catalytic activity.

The three SMOs are *p*-type semiconductors (Ahmad et al. 2018; Jiang et al. 2018; Quang et al. 2018) and accordingly rich in holes. These holes act as good acceptors to the electrons of the cellulose and hemicellulose function groups, which initiates the breakdown of the polymeric unites (Ayoman and Hosseini 2016). Moreover, the presence of vacant d-orbitals of the transition metal cations ($3d^7$ in Co^{2+}, $3d^8$ in Ni^{2+}, and $3d^9$ in Cu^{2+}) play an important role as electron receptors too (Alizadeh-Gheshlaghi et al. 2012).

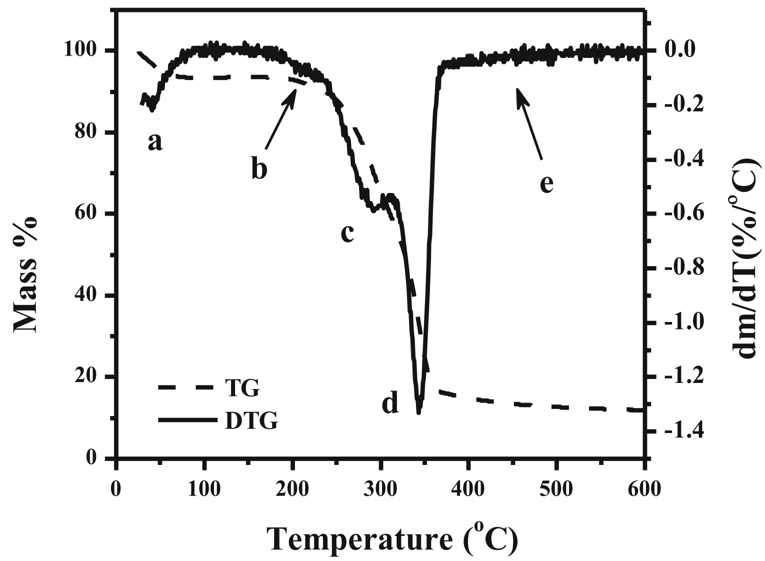

Fig. 3 TG and DTG curves of SCB at heating rate 5 °C/min

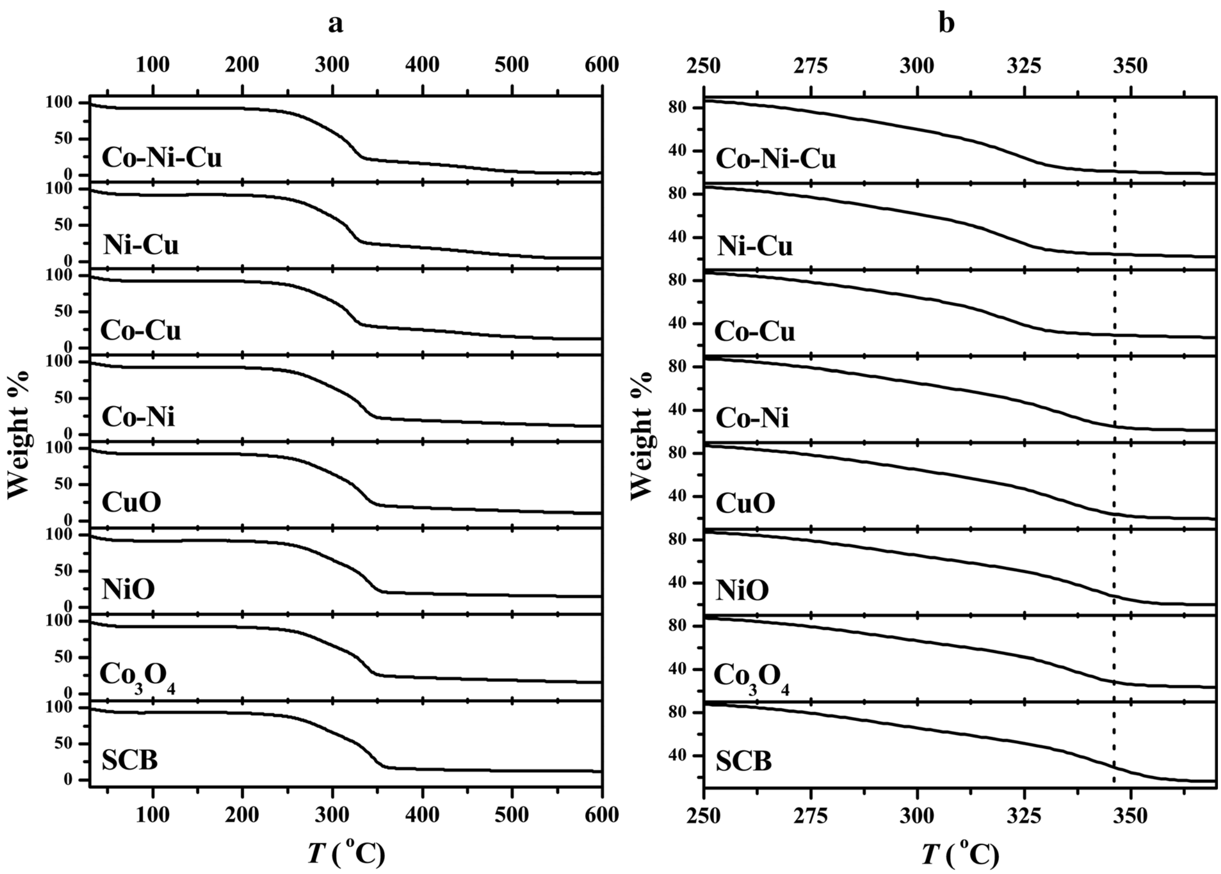

Fig. 4 TG curves of the PSCB with and without Co, Ni, and Cu SMO and MMO NPs. **a** Over the whole temperature range of study. **b** Temperature scale zoomed within 250–375 °C, respectively. The dashed line in **b** represents T_m of plain SCB

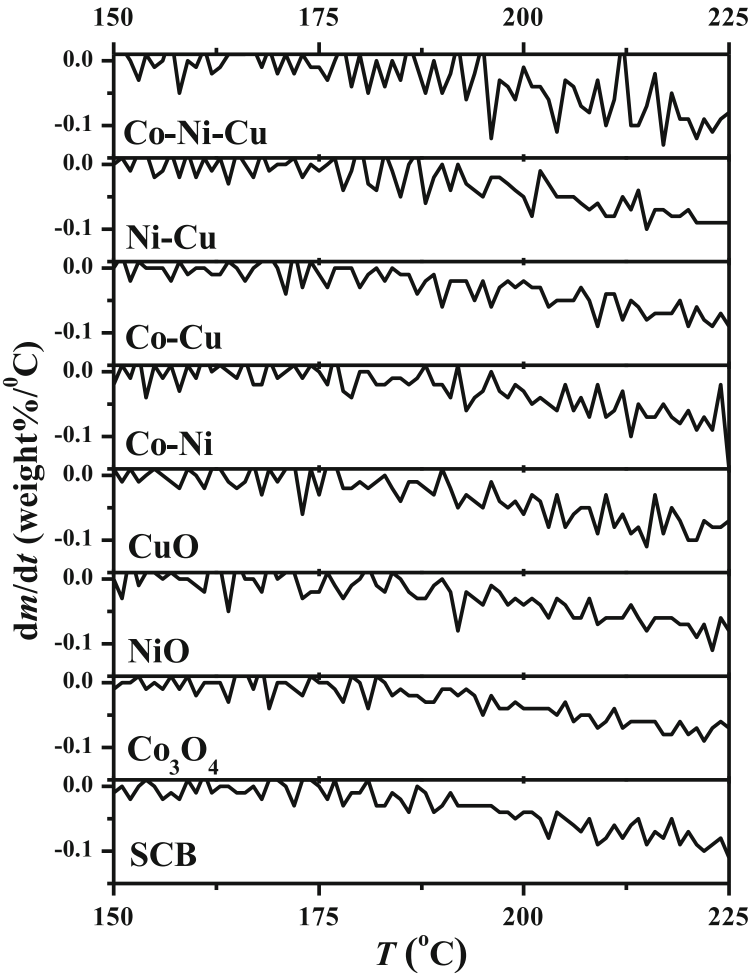

Fig. 5 The DTG curves of PSCB in absence and presence of SMO and MMO NPs within temperature range of 150–225 °C

The catalysis of pyrolysis by NPs is heterogeneous catalysis that involves adsorption of the reactant function groups at active sites of the catalyst surface. An unpublished work of us (in process of writing) shows how specifically CuO NPs have superior adsorption affinity compared to NiO and Co_3O_4 towards Congo Red dye, which is an anionic organic molecule. The negatively charged function groups of Congo Red mimic the electron-rich centers of cellulose and hemicellulose, which may give an explanation of the odd catalytic activity of CuO to our bagasse pyrolysis.

Catalytic activity of the MMO NPs

According to the DTG curves and the data shown in Table 2, MMO NPs show more catalytic activity towards PSCB than MMO. The T_m values indicate that all MMO NPs of this study are more catalytic to cellulose and hemicellulose thermal degradation than SMO NPs, even though the overall specific surface areas of the double MMO NPs are much smaller than those of the SMO NPs. This can be attributed to the dual or multiple functionality of the components constituting the double MMO NPs, which sums up to result in synergetic catalysis (Gawande et al. 2012; Wachs and Routray 2012). Moreover, the unit cell of the double and triple MMO crystallites of Co, Ni, and Cu possess two important characteristics that induce synergism in the catalytic activity of the MMO NPs. On one hand, it is the blend of the vacant $3d^7$, $3d^8$, and $3d^9$ orbitals. On the other hand, the crystal distortions (John-Teller distortions) due to the mutual doping of the two/three cations into the crystals of the double/triple MMO produces electron and hole trapping centers. Both phenomena raise the ability of the crystal to deal with the

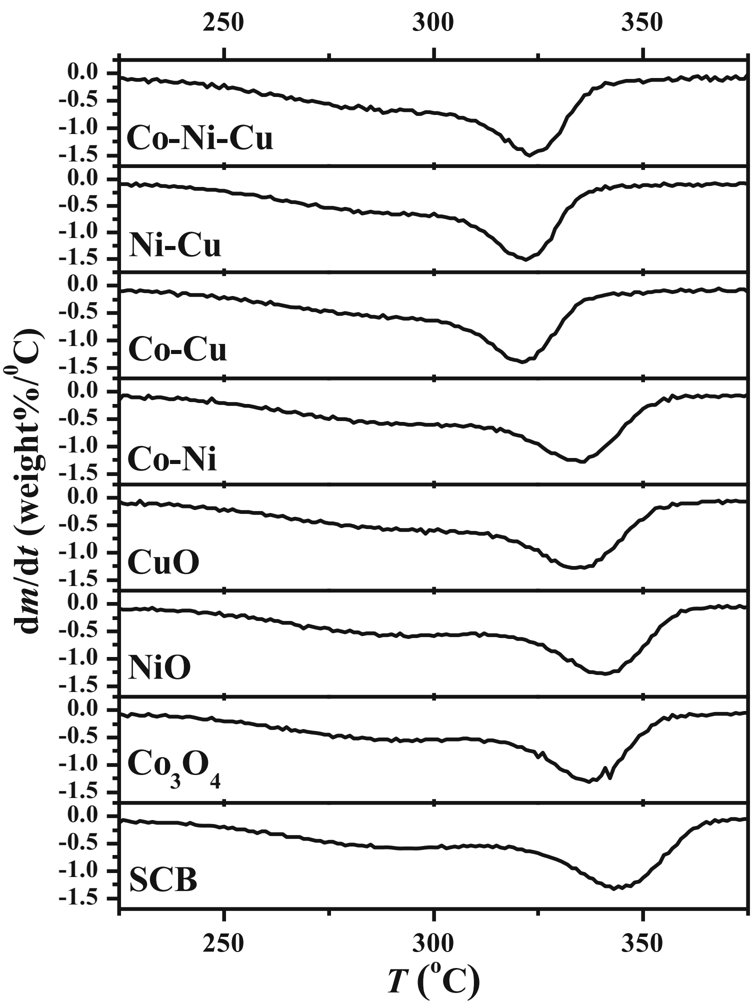

Fig. 6 The DTG curves within temperature range of 225–375 °C for cellulose and hemicellulose degradation during the PSCB in absence and presence of the SMO and MMO NPs

electrons of the reactant function groups and accordingly boost the catalytic activity (Alizadeh-Gheshlaghi et al. 2012).

The DTG curves show that the highest catalytic activities belong to those MMOs of the Cu content. The Cu-containing MMO NPs not only catalyze cellulose and hemicellulose thermal degradation, but also catalyze the stubborn lignin thermal degradation, which is not overcome by any of the other SMO or MMO NPs. As discussed above in "Catalytic activity of the SMO NPs," we attribute unique high activity of the Cu-containing MMO NPs to the high affinity and adsorption capacity of Cu oxides towards electron-rich centers. Despite this surpassing catalytic activity, Cu-containing MMO NPs lack the advantage of selectivity towards cellulose and hemicellulose and induce thermal degradation of lignin alongside.

Kinetics of the PSCB in presence and absence of the SMO and MMO NPs

We applied kinetic modeling to judge the catalytic activity towards the PSCB as a whole. The kinetic parameters were estimated by applying Coats-Redfern model in the form of Eqs. 3 through 5 (Ceylan and Topçu 2014; Marini et al. 1979):

$$\ln G(\alpha) = -\frac{E}{\mathrm{R}T} + \ln\left(\frac{\mathrm{AR}}{\beta E}\right) \quad (3)$$

$$G(\alpha) = -\frac{\ln(1-\alpha)}{T^2} \ \text{(for n = 1)} \quad (4)$$

$$G(\alpha) = \frac{1-(1-\alpha)^{1-n}}{(1-n)T^2} \ \text{(for n}\neq 1\text{)} \quad (5)$$

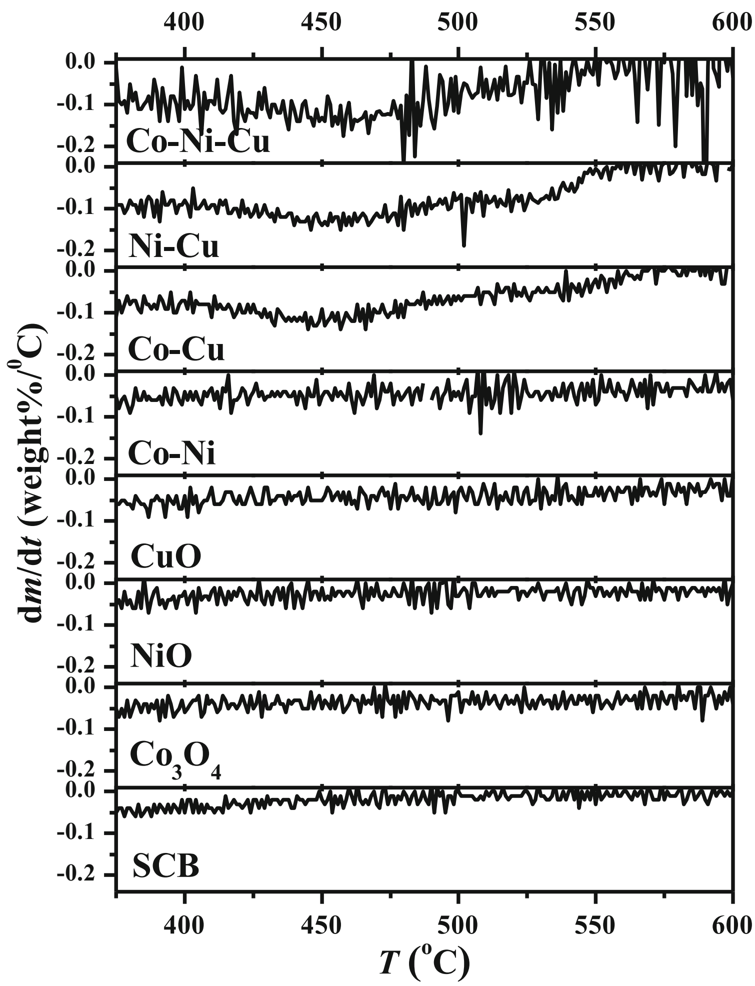

Fig. 7 The DTG curves within temperature range of 375–600 °C for lignin degradation during the PSCB in absence and presence of the SMO and MMO NPs

where $G(\alpha)$ is called the integral function of Coats-Redfern model, α is the decomposition fraction at time t, A is the pre-exponential factor, E is activation energy, R is the universal gas constant, and n is the order of the reaction.

This kinetic study was based on the data obtained from thermogravimetric analysis where α is maintained from 0.2 to 0.8. Figure S3 (Supplementary Information) shows the linear plots of $\ln[G(\alpha)]$ versus $1/T$ for the PSCB with and without catalysts where the slope is the activation energy (E_a). The reaction order $n = 2$ gave the best fit with the highest linear regression factor (R^2) for the PSCB with and without catalyst. Table 2 illustrates the kinetic data, which shows the influence of the SMO and MMO NPs on the PSCB. A considerable reduction in E_a was reached by the addition of the metal oxide NPs. The reduction in E_a and therefore the enhancement in the catalytic activity took the order of SMO NPs < double MMO NPs < triple MMO NPs. Co-Ni-Cu MMO NPs gave the largest reduction in E_a (highest catalytic activity). This result agrees with the behavior of the shifts in the DTG peaks.

Conclusions

Co, Ni, and Cu SMO and MMO NPs show catalytic activity towards PSCB as they reduce activation energy of PSCB. More specifically, temperatures of cellulose and hemicellulose thermal degradation descend in presence of the oxide NPs. MMO NPs show more catalytic activity than SMO NPs for cellulose and hemicellulose thermal degradation. Combination of more than one of Co, Ni, and Cu in the oxide gives a blend of vacant d-orbitals, hole-rich p-type semiconductors, and multifunctional catalytic surface, which all result in synergism in the catalytic activity. Presence of Cu in SMO and MMO NPs increases their catalytic activities compared to their Cu-free analogues. This behavior is attributed to the exceptional adsorption capacity of CuO to the electron-rich function groups/centers of the reactants (studied by unpublished work). Lignin degraded over a wide range of high temperature in absence and presence of the oxide NPs, except NPs of Cu-containing MMOs. This can be considered as a selective enhancement of the catalysis of cellulose and hemicellulose thermal degradation versus lignin degradation. This enhancement increased from SMO to MMO NPs. On the other hand, Cu-containing double and triple MMO NPs are so catalytically active that they catalyze lignin thermal degradation along with cellulose and hemicellulose. This high catalytic activity and lack of selectivity have to be due to the odd adsorption capacity and affinity of Cu oxides towards electron-rich center, as referred to above.

Funding information Financial support granted by the Ministry of Scientific Research and the Academy of Scientific Research and Technology (ASRT) through the program Scientists of Next Generation-2015 (SNG-5).

Compliance with ethical standards

Conflict of interest The authors declare that they have no conflict of interest.

References

Ahmad J, Majid K, Dar MA (2018) Controlled synthesis of p-type NiO/n-type GO nanocomposite with enhanced photocatalytic activity and study of temperature effect on the photocatalytic activity of the nanocomposite. Appl Surf Sci 457:417–426. https://doi.org/10.1016/j.apsusc.2018.06.200

Ali G, Park YJ, Kim JW, Cho SO (2018) A Green, general, and ultrafast route for the synthesis of diverse Metal oxide nanoparticles with controllable sizes and enhanced catalytic activity. ACS Appl Nano Mater 1:6112–6122. https://doi.org/10.1021/acsanm.8b01220

Alizadeh-Gheshlaghi E, Shaabani B, Khodayari A, Azizian-Kalandaragh Y, Rahimi R (2012) Investigation of the catalytic activity of nano-sized CuO, Co3O4 and CuCo2O4 powders on thermal decomposition of ammonium perchlorate. Powder Technol 217:330–339. https://doi.org/10.1016/j.powtec.2011.10.045

Arregi A, Lopez G, Amutio M, Barbarias I, Santamaria L, Bilbao J, Olazar M (2018) Kinetic study of the catalytic reforming of biomass pyrolysis volatiles over a commercial Ni/Al2O3 catalyst. Int J Hydrogen Energy 43:12023–12033. https://doi.org/10.1016/j.ijhydene.2018.05.032

Ayoman E, Hosseini SG (2016) Synthesis of CuO nanopowders by high-energy ball-milling method and investigation of their catalytic activity on thermal decomposition of ammonium perchlorate particles. J Therm Anal Calorim 123:1213–1224. https://doi.org/10.1007/s10973-015-5059-1

Balasundram V, Ibrahim N, Kasmani RM, Isha R, Abd Hamid MK, Hasbullah H, Ali RR (2018a) Catalytic upgrading of sugarcane bagasse pyrolysis vapours over rare earth metal (Ce) loaded HZSM-5: effect of catalyst to biomass ratio on the organic compounds in pyrolysis oil. Appl Energy 220: 787–799. https://doi.org/10.1016/j.apenergy.2018.03.141

Balasundram V, Zaman KK, Ibrahim N, Kasmani RM, Isha R, Hamid MKA, Hasbullah H (2018b) Catalytic upgrading of pyrolysis vapours over metal modified HZSM-5 via in-situ pyrolysis of sugarcane bagasse: effect of nickel to cerium ratio on HZSM-5. J Anal Appl Pyrolysis 134:309–325. https://doi.org/10.1016/j.jaap.2018.06.021

Banković-Ilić IB, Miladinović MR, Stamenković OS, Veljković VB (2017) Application of nano CaO–based catalysts in biodiesel synthesis. Renew Sustain Energy Rev 72:746–760

Bedoic R et al (2019) Green biomass to biogas - a study on anaerobic digestion of residue grass. J Clean Prod 213:700–709. https://doi.org/10.1016/j.jclepro.2018.12.224

Cardoso ART, Conrado NM, Krause MC, Bjerk TR, Krause LC, Caramao EB (2019) Chemical characterization of the bio-oil obtained by catalytic pyrolysis of sugarcane bagasse (industrial waste) from the species Erianthus Arundinaceus. J Environ Chem Eng 7:7. https://doi.org/10.1016/j.jece.2019.102970

Cen HY, Wan L, Zhu J, Li Y, Li X, Zhu Y, Weng H, Wu W, Yin W, Xu C, Bao Y, Feng L, Shou J, He Y (2019) Dynamic monitoring of biomass of rice under different nitrogen treatments using a lightweight UAV with dual image-frame snapshot cameras. Plant Methods 15:16–16. https://doi.org/10.1186/s13007-019-0418-8

Ceylan S, Topçu Y (2014) Pyrolysis kinetics of hazelnut husk using thermogravimetric analysis. Bioresour Technol 156: 182–188

Chang R et al (2018) Production of bio-based p-xylene via catalytic pyrolysis of biomass over metal oxide-modified HZSM-5 zeolites. J Chem Technol Biotechnol 93:3292–3301. https://doi.org/10.1002/jctb.5691

Dahunsi SO (2019) Mechanical pretreatment of lignocelluloses for enhanced biogas production: methane yield prediction from biomass structural components. Bioresour Technol 280:18–26. https://doi.org/10.1016/j.biortech.2019.02.006

Deboni TL, Simioni FJ, Brand MA, Lopes GP (2019) Evolution of the quality of forest biomass for energy generation in a cogeneration plant. Renew Energy 135:1291–1302. https://doi.org/10.1016/j.renene.2018.09.039

Dhanalakshmi CS, Madhu P (2019) Utilization possibilities of *Albizia amara* as a source of biomass energy for bio-oil in pyrolysis process. Energy Sources Part A 41:1908–1919. https://doi.org/10.1080/15567036.2018.1549168

Donar YO, Sinag A (2016) Catalytic effect of tin oxide nanoparticles on cellulose pyrolysis. J Anal Appl Pyrolysis 119:69–74. https://doi.org/10.1016/j.jaap.2016.03.016

Elbaba IF, Williams PT (2013) High yield hydrogen from the pyrolysis-catalytic gasification of waste tyres with a nickel/

dolomite catalyst. Fuel 106:528–536. https://doi.org/10.1016/j.fuel.2012.12.067

El-Sayed SA, Mostafa ME (2015) Kinetic parameters determination of biomass pyrolysis fuels using TGA and DTA techniques. Waste Biomass Valorization 6:401–415

Garcıa-Perez M, Chaala A, Yang J, Roy C (2001) Co-pyrolysis of sugarcane bagasse with petroleum residue. Part I: thermogravimetric analysis. Fuel 80:1245–1258

Gawande MB, Pandey RK, Jayaram RV (2012) Role of mixed metal oxides in catalysis science—versatile applications in organic synthesis. Catal Sci Technol 2:1113–1125

Ghorbannezhad P, Firouzabadi MD, Ghasemian A (2018) Catalytic fast pyrolysis of sugarcane bagasse pith with HZSM-5 catalyst using tandem micro-reactor-GC-MS energy sources part A-recovery. Util Environ Eff 40:15–21. https://doi.org/10.1080/15567036.2017.1381785

Ghorbarmezhad P, Firouzabadi MD, Ghasemian A, de Wild PJ, Heeres HJ (2018) Sugarcane bagasse ex-situ catalytic fast pyrolysis for the production of benzene, Toluene and Xylenes (BTX). J Anal Appl Pyrolysis 131:1–8. https://doi.org/10.1016/j.jaap.2018.02.019

Gnanasekaran L, Hemamalini R, Saravanan R, Ravichandran K, Gracia F, Agarwal S, Gupta VK (2017) Synthesis and characterization of metal oxides (CeO2, CuO, NiO, Mn3O4, SnO2 and ZnO) nanoparticles as photo catalysts for degradation of textile dyes. J Photochem Photobiol B Biol 173:43–49

Hassan HB, Tammam RH (2018) Preparation of Ni-metal oxide nanocomposites and their role in enhancing the electrocatalytic activity towards methanol and ethanol. Solid State Ionics 320:325–338. https://doi.org/10.1016/j.ssi.2018.03.020

Hassan E, Elsayed I, Eseyin A (2016) Production high yields of aromatic hydrocarbons through catalytic fast pyrolysis of torrefied wood and polystyrene. Fuel 174:317–324. https://doi.org/10.1016/j.fuel.2016.02.031

Hernando H et al (2017) Biomass catalytic fast pyrolysis over hierarchical ZSM-5 and beta zeolites modified with mg and Zn oxides. Biomass Convers Biorefinery 7:289–304. https://doi.org/10.1007/s13399-017-0266-6

Ikaheimo J, Pursiheimo E, Kiviluoma J, Holttinen H (2019) Role of power to liquids and biomass to liquids in a nearly renewable energy system. IET Renew Power Gener 13:1179–1189. https://doi.org/10.1049/iet-rpg.2018.5007

Ismail AM, Emara MM, El din Kassem TS, Moussa MA (2017) How assembly matters to catalysis and thermal conductivity mediated by CuO nanoparticles. Nanotechnology 28:075705

Janke L et al (2019) Ensiling fermentation reveals pre-treatment effects for anaerobic digestion of sugarcane biomass: an assessment of ensiling additives on methane potential. Bioresour Technol 279:398–403. https://doi.org/10.1016/j.biortech.2019.01.143

Jiang TF et al (2018) Cu2O@CuO core-shell nanoparticles as photocathode for p-type dye sensitized solar cell. J Alloys Compd 769:605–610. https://doi.org/10.1016/j.jallcom.2018.07.328

Khan A, Liao Z, Liu Y, Jawad A, Ifthikar J, Chen Z (2017) Synergistic degradation of phenols using peroxymonosulfate activated by CuO-Co3O4@ MnO2 nanocatalyst. J Hazard Mater 329:262–271

Khiari B, Jeguirim M, Limousy L, Bennici S (2019) Biomass derived chars for energy applications. Renew Sust Energ Rev 108:253–273. https://doi.org/10.1016/j.rser.2019.03.057

Kuan WH, Huang YF, Chang CC, Lo SL (2013) Catalytic pyrolysis of sugarcane bagasse by using microwave heating. Bioresour Technol 146:324–329. https://doi.org/10.1016/j.biortech.2013.07.079

Kumar P, Agrawal KV, Tsapatsis M, Mkhoyan KA (2015) Quantification of thickness and wrinkling of exfoliated two-dimensional zeolite nanosheets. Nat Commun 6:7–7. https://doi.org/10.1038/ncomms8128

Li J-F, Xiao B, Du L-J, Yan R, Liang TD (2008) Preparation of nano-NiO particles and evaluation of their catalytic activity in pyrolyzing cellulose. J Fuel Chem Technol 36:42–47. https://doi.org/10.1016/s1872-5813(08)60010-9

Li C et al (2017) Shape-controlled CeO2 nanoparticles: stability and activity in the catalyzed HCl oxidation reaction. ACS Catalysis 7:6453–6463

Li KJ et al (2018) A generic method for preparing hollow mesoporous silica catalytic nanoreactors with metal oxide nanoparticles inside their cavities. Angew Chem-Int Edit 57:16458–16463. https://doi.org/10.1002/anie.201810777

Li FH, Srivatsa SC, Bhattacharya S (2019) A review on catalytic pyrolysis of microalgae to high-quality bio-oil with low oxygeneous and nitrogenous compounds. Renew Sust Energ Rev 108:481–497. https://doi.org/10.1016/j.rser.2019.03.026

Liu Q, Wang S, Luo Z, Cen K (2008) Catalysis mechanism study of potassium salts on cellulose pyrolysis by using TGA-FTIR analysis. J Chem Eng Jpn 41:1133–1142

Liu FJ et al (2013) Generalized and high temperature synthesis of a series of crystalline mesoporous metal oxides based nanocomposites with enhanced catalytic activities for benzene combustion. J Mater Chem A 1:4089–4096. https://doi.org/10.1039/c3ta01505j

Lopez-Rodriguez M et al (2019) Assessment of multi-step processes for an integral use of the biomass of the marine microalga Amphidinium carterae. Bioresour Technol 282:370–377. https://doi.org/10.1016/j.biortech.2019.03.041

Ma JG et al (2019) Rare-earth metal oxide hybridized PtFe nanocrystals synthesized via microfluidic process for enhanced electrochemical catalytic performance. Electrochim Acta 299:80–88. https://doi.org/10.1016/j.electacta.2018.12.132

Marini A, Berbenni V, Flor G (1979) Kinetic parameters from thermogravimetric data. Zeitschrift für Naturforschung A 34:661–663

Mohapatra S, Mishra SS, Das SK, Thatoi H (2019) Influence of reactors, microbial carbohydrate uptake, and metabolic pathways on ethanol production from grass biomass: a review. Int J Energy Res 43:1615–1646. https://doi.org/10.1002/er.4294

Mortari DA, Ávila I, Santos AM, Crnkovic PCGM (2010) Study of thermal decomposition of ignition temperature of bagasse, coal and their blends. Engenharia Térmica:81–88

Motaung T, Anandjiwala R (2015) Effect of alkali and acid treatment on thermal degradation kinetics of sugar cane bagasse. Ind Crops Prod 74:472–477

Mothé CG, de Miranda IC (2009) Characterization of sugarcane and coconut fibers by thermal analysis and FTIR. J Therm Anal Calorim 97:661

Murugappan K, Mukarakate C, Budhi S, Shetty M, Nimlos MR, Roman-Leshkov Y (2016) Supported molybdenum oxides as effective catalysts for the catalytic fast pyrolysis of lignocellulosic biomass. Green Chem 18:5548–5557. https://doi.org/10.1039/c6gc01189f

Muthuvinothini A, Stella S (2019) Green synthesis of metal oxide nanoparticles and their catalytic activity for the reduction of aldehydes. Process Biochem 77:48–56. https://doi.org/10.1016/j.procbio.2018.12.001

Nguyen TS, He SB, Raman G, Seshan K (2016) Catalytic hydropyrolysis of lignocellulosic biomass over dual Na2CO3/Al2O3 and Pt/Al2O3 catalysts using n-butane at ambient pressure. Chem Eng J 299:415–419. https://doi.org/10.1016/j.cej.2016.04.104

Ozbay N, Yargic AS, Sahin RZY, Yaman E (2019) Valorization of banana peel waste via in-situ catalytic pyrolysis using Al-modified SBA-15. Renew Energy 140:633–646. https://doi.org/10.1016/j.renene.2019.03.071

Paunovic O, Pap S, Maletic S, Taggart MA, Boskovic N, Sekulic MT (2019) Ionisable emerging pharmaceutical adsorption onto microwave functionalised biochar derived from novel lignocellulosic waste biomass. J Colloid Interface Sci 547:350–360. https://doi.org/10.1016/j.jcis.2019.04.011

Prager F, Paczkowski S, Sailer G, Derkyi NSA, Pelz S (2019) Biomass sources for a sustainable energy supply in Ghana - a case study for Sunyani. Renew Sust Energ Rev 107:413–424. https://doi.org/10.1016/j.rser.2019.03.016

Quang PL, Cuong ND, Hoa TT, Long HT, Hung CM, Le DTT, Hieu NV (2018) Simple post-synthesis of mesoporous p-type Co3O4 nanochains for enhanced H2S gas sensing performance. Sensors Actuators B Chem 270:158–166. https://doi.org/10.1016/j.snb.2018.05.026

Said M, John G, Mhilu C, Manyele S (2013) Fast pyrolysis and kinetics of sugarcane bagasse in energy recovery. In: Climate-Smart Technologies. Springer, pp 415–424

Shen DK, Gu S, Bridgwater AV (2010) The thermal performance of the polysaccharides extracted from hardwood: cellulose and hemicellulose. Carbohydr Polym 82:39–45. https://doi.org/10.1016/j.carbpol.2010.04.018

Stefanidis SD, Kalogiannis KG, Iliopoulou EF, Michailof CM, Pilavachi PA, Lappas AA (2014) A study of lignocellulosic biomass pyrolysis via the pyrolysis of cellulose, hemicellulose and lignin. J Anal Appl Pyrolysis 105:143–150

Thomas P, Lai CW, Bin Johan MR (2019) Recent developments in biomass-derived carbon as a potential sustainable material for super-capacitor-based energy storage and environmental applications. J Anal Appl Pyrolysis 140:54–85. https://doi.org/10.1016/j.jaap.2019.03.021

Wachs IE, Routray K (2012) Catalysis science of bulk mixed oxides. ACS Catalysis 2:1235–1246. https://doi.org/10.1021/cs2005482

Weldekidan H, Strezov V, Kan T, Kumar R, He J, Town G (2019) Solar assisted catalytic pyrolysis of chicken-litter waste with in-situ and ex-situ loading of CaO and char. Fuel 246:408–416. https://doi.org/10.1016/j.fuel.2019.02.135

Yang Y, Jin Y, He H, Wang Q, Tu Y, Lu H, Ye Z (2010) Dopant-induced shape evolution of colloidal nanocrystals: the case of zinc oxide. J Am Chem Soc 132:13381–13394

Zhu H, Han D, Meng Z, Wu D, Zhang C (2011) Preparation and thermal conductivity of CuO nanofluid via a wet chemical method. Nanoscale Res Lett 6:181